# Role of sodium sulfate in electrical conductivity and structure of lignin-derived carbons

Seth Kane, David B. Hodge, Brian Saulnier, Villő Enikő Bécsy-Jakab, Dilara N. Dülger, Cecily Ryan

# Role of sodium sulfate in electrical conductivity and structure of lignin-derived carbons

Seth Kane[a,*], David B. Hodge[b], Brian Saulnier[b], Villő Enikő Bécsy-Jakab[b], Dilara N. Dülger[b], Cecily Ryan[a]

[a]*Montana State University, Bozeman, MT 59717, United States, Mechanical and Industrial Engineering*
[b]*Montana State University, Bozeman, MT 59717, United States, Chemical and Biological Engineering*

## Abstract

Lignin is a promising renewable alternative to fossil fuels for producing carbon materials such as carbon fibers, activated carbons, or carbon black. Despite extensive research, lignin-derived carbon materials show limited graphitization relative to comparable petroleum-derived carbons. Further, lignin-derived carbons show high variation in graphitization and electrical conductivity depending on the source of the lignin. Herein, nine lignins, derived from various feedstocks and isolation procedures, are pyrolyzed to produce biochar at 1100 °C. These lignins have a range of chemical compositions, carbon structures, and particle sizes. As a result, the pyrolysis behavior of these lignins varies, with powdered, clumped powder, and "foam" biochar morphologies resulting from finely powdered lignin. The produced biochars vary widely in both electrical conductivity, from 0.19 to

[*]**Corresponding author**, sethkane@montana.edu, (907)750-6364.
**Current address**: skane@ucdavis.edu, University of California - Davis, Civil and Environmental Engineering, 2001 Ghausi Hall Davis, CA 95616, USA

19 S/cm, and in-plane graphitic crystallite size, from 3.4 to 41.2 Å. A significant decrease in electrical conductivity is identified when $Na_2SO_4$ is removed from lignin, accompanied by an increase in graphitic crystallite size. Based on this finding, a quadratic relationship between biochar graphitic crystallite aspect ratio and electrical conductivity is proposed that builds on established quasi-percolation models for biochar electrical conductivity.

*Keywords:* Biochar, biocarbon, pyrolysis, non-graphitizing carbon, graphitzation.

---

## 1. Introduction

Developing renewable alternatives to petroleum-derived materials is critical to reducing our society's reliance on fossil fuels. Of particular interest are carbon materials, such as carbon black, carbon fibers, and artificial graphite, whose application is expected to grow rapidly in the coming decades [1]. Lignin looks to be a promising alternative feedstock to petroleum due to its high aromatic carbon content [2]. Further, 50-100 Mt of lignin are isolated annually as a byproduct of paper-making and biorefinery industries [3], which is anticipated to grow as cellulosic biorefineries continue to expand in the coming decade [4]. However, economic factors primarily limit upcycling of lignin waste streams [5]. As carbon materials are considered some of the most valuable products of lignin [6], the development of simple processes to convert this lignin to renewable carbon materials has the potential to both reduce reliance on petroleum products and upcycle this important waste stream.

Lignin-derived carbon materials can be produced via pyrolysis and have been extensively studied [2, 7, 8, 9, 10, 11]. During pyrolysis, oxygen and hydrogen present in lignin react with carbon to form liquid and gas decomposition products, reducing the content of hydrogen and oxygen in the solid phase [12]. The resulting solid material has a graphitic carbon structure, porous morphology, and high electrical conductivity. With optimal processing conditions and feedstock properties, lignin-derived carbons have the potential to replace petroleum-derived materials such as carbon black [11, 13], carbon fibers [7], and activated carbons[14]. Lignin-derived biochars and biocarbons have been examined for a broad set of applications, including electrically conductive plastic additives, replacements for carbon black, and active materials in battery electrodes [11, 13, 15, 16]. Lignin-derived carbons are limited by lower graphitization and increased defects relative to petroleum-derived carbon materials [7, 13, 17, 18]. Further, a large range of electrical conductivity is observed for biochars graphitized at around 1000 °C, from 0.009 S/cm to 62.96 S/cm for lignins isolated with different processes [10, 19].

These past studies point to lignin as a promising feedstock for various carbon materials; however, its performance is consistently limited by lower graphitization than petroleum-derived carbon materials [7, 13, 17, 18]. Further, wide ranges of electrical conductivity and graphitization have been reported for carbons derived from lignins isolated with different processes. Since graphitization of lignin-derived carbons does not continue to increase above pyrolysis temperatures of approximately 1000 °C, graphitization cannot typically be increased with

higher carbonization temperatures [7, 20, 21]. Lignin molecular weight, inorganic content, and particle size have been identified as critical factors that influence the graphitization of lignin during pyrolysis [7, 10, 15]. Past studies differ in the role that common inorganic compounds, such as sodium sulfate ($Na_2SO_4$) present in kraft lignins, play in lignin pyrolysis. Some studies have proposed that $Na_2SO_4$ catalyzes the formation of graphitic structures, while others propose that $Na_2SO_4$ inhibits the formation of graphitic structures [22, 23, 24, 25], while recent reviews have highlighted this as an area in need of study [18].

This study investigates the role of different lignin isolation procedures, dominant monomers, parameters, and feedstocks in the graphitization of lignin-derived biochar. Lignins from nine different isolation approaches are characterized for chemical structure, molecular weight, and thermal transitions. These lignins are then pyrolyzed to form biochar at 1100 °C, and the morphology, chemical composition, carbon structure, and electrical conductivity of these biochar are investigated. First, the relationship between lignin processing and biochar carbon structure is examined. We hypothesize that lignin oxygen content, which is expected to be strongly driven by the ratio of monomers in the lignin, will significantly affect biochar carbon structure and electrical conductivity. Next, the role that $Na_2SO_4$ plays in lignin pyrolysis is tested directly by removing $Na_2SO_4$ from lignin. We hypothesize that the presence of $Na_2SO_4$ in lignin will increase biochar graphitization. This work sheds light on how lignin properties impact carbon structures formed during pyrolysis and can inform feedstock optimization to utilize this important waste stream to create renewable and high-performance carbon materials.

Table 1: Summary of lignin isolation methods and molecular weights (weight average (Mn), number average (Mn), and polydispersity index (PDI)). Listed temperatures are the maximum processing temperatures.

| Name (Abbreviation) | Feedstock | Process type | Max. process temp. (°C) | Mw (Da) | Mn (Da) | PDI (Mw/Mn) |
|---|---|---|---|---|---|---|
| TCI Alkaline (TA) | Wood | Commercial, Lignosulfonate | Unk. | 60000 [27] | - | - |
| TCI Dealkaline (TD) | Wood | Commercial, Lignosulfonate | Unk. | 60000 [27, 28] | - | - |
| Sigma Alkali (SA) | Softwood | Commercial, Kraft | Unk. | 28000 [28] | 5000 | 5.6 |
| Alkali-corn140 (AC140) | Corn stover | Alkali pretreatment, acidification | 140 | 11400 | 3100 | 3.7 |
| alkali-poplar150 (AP150) | Poplar | Alkali pretreatment, acidification | 150 | 12100 | 3600 | 3.4 |
| Alkali-poplar95 (AP95) | Poplar | Alkali pretreatment, acidification | 95 | 8000 [29] | 4300 | 5.3 |
| Hydrolysis-corn (HC) | Corn stover | Alkali pretreatment, enzymatic hydrolysis | 150 | 10000 | 4100 | 2.4 |
| Alkali-poplar115 (AP115) | Poplar | Alkali pretreatment, acidification | 115 | 8700 | 3500 | 2.5 |
| Alkali -poplar145 (AP145) | Poplar | Alkali pretreatment, acidification | 145 | 8400 | 3200 | 2.7 |

## 2. Materials and Methods

### *2.1. Lignin sources and isolation*

Three commercial lignins were obtained: alkaline lignin (TCI America, Portland, OR, USA, product # L0082), dealkaline lignin (TCI America, Portland, OR, USA, product # L0045), and alkali lignin (Sigma-Aldrich, Inc., St. Louis, MO, USA, product # 370959). In addition, six laboratory-isolated lignins were produced from hybrid poplar or corn stover using various approaches for lignin isolation and recovery. These lignins vary in feedstock, isolation process, and isolation parameters (Table 1). These processes are described in detail in the Supplemental Information. After isolation, alkali-corn140, alkali-poplar150, alkali-poplar115, and alkali-poplar145 were washed with deionized water to remove $Na_2SO_4$, following previously applied procedures [26].

Three different treatments were used to reduce lignin particle size prior to

pyrolysis to examine the impact of particle size on lignin pyrolysis. The commercial lignins (TCI Alkaline, TCI Dealkaline, and Sigma Alkali) are pyrolyzed as provided. Alkali-poplar150, alkali-corn140, and alkali-poplar95 were ball milled (Retsch Mixer Mill 400) for 3 min at 30 Hz (1800 rpm). Alklai-poplar115, alkali-poplar145, and hydrolysis-corn were ground with a pestle and mortar for 3 min.

### *2.2. Biochar production*

All nine lignins were converted to biochar via pyrolysis in a tube furnace. Prior to pyrolysis or analysis, all lignins were stored in a drying oven at 105 °C for at least 24 h to reduce moisture content. Approximately 500 mg of lignin was placed in an alumina boat (100 mm × 20 mm × 13 mm) within the tube furnace (Lindberg/Blue M Mini Mite) fitted with an alumina tube. The tube furnace was purged with nitrogen at 100 mL $min^{-1}$ for 10 min prior to heating. During heating, the purge rate for nitrogen was reduced to 30 mL $min^{-1}$, and the lignin was heated at 10 °C $min^{-1}$ from room temperature to 1100 °C, held for 1 h, and then allowed to cool to room temperature. The maximum pyrolysis temperature of 1100 °C was selected as past studies show limited increases in electrical conductivity at higher pyrolysis temperatures for non-graphitizing feedstocks, such as lignin [21, 30].

After pyrolysis, the biochar was ball milled (Retsch Mixer Mill 400 with a 50 mL steel jar and a 25 mm steel ball) for 3 min at 30 Hz (1800 rpm). Biochar was stored in a drying oven at 105 °C until analysis. A single batch of biochar was produced for each lignin type. Samples were weighed both before and after pyrolysis to determine pyrolysis yield.

### *2.3. Sodium sulfate removal*

As a secondary experiment, the impact of lignin $Na_2SO_4$ content was directly studied by removing $Na_2SO_4$ from alkali-poplar95 lignin. To this end, the alkali-poplar95 lignin was triple washed at a mass ratio of 1 part original mass to 50 parts deionized water to remove $Na_2SO_4$ and centrifuged to separate after each washing cycle following established procedures [26]. Lignin was freeze-dried after washing and then stored at 105 °C until pyrolysis. Biochars were then prepared with this lignin and compared against unwashed alkali-poplar95 biochar. Both biochars and washing residues were measured with X-ray diffraction (XRD) and energy dispersive x-ray (EDX) spectroscopy, as described in Section 2.4 to verify the removal of $Na_2SO_4$. For this set of experiments, biochar samples were produced in triplicate.

### *2.4. Lignin and biochar characterization*

Biochar pyrolysis conditions were simulated in a thermogravimetric analyzer (TGA, TA Instruments Q8000IR) to examine the weight loss as a function of temperature. Approximately 5 mg of each lignin was placed in a HT-platinum TGA pan and heated from 30 °C to 1000 °C at a rate of 10 °C $min^{-1}$ under a 30 mL $min^{-1}$ flow of nitrogen gas. Lignin thermal transitions at low temperatures were examined with differential scanning calorimetry (DSC, TA Instruments Discovery 2500). For DSC, approximately 5 mg of each lignin was placed in a TZero DSC pan and heated from 30 °C to 400 °C at a rate of 10 °C $min^{-1}$.

Atomic species present in biochar were examined with EDX spectroscopy with an Oxford Ultim Max EDX detector on a Zeiss SUPRA 55VP field emis-

sion scanning electron microscope (FESEM). Based on the EDX results (Supplemental Figure S7), C, H, N, S, Na, Mg, Ca, and K were selected for quantified analysis. The C, H, N, and S content of all lignins and biochars were characterized with combustion analysis by Atlantic Microlab Inc. (Norcross, Georgia, USA). Lignin and biochar Na, Mg, Ca, and K content were characterized with inductively coupled plasma optical emission spectrometry (ICP-OES). Biochar and lignin samples were digested in trace metal grade $HNO_3$ (Fisher Scientific, product #A509P500, Pittsburgh, PA USA) on a Mars6 iWave digester at 220 °C with a ramp time of 15 min, a hold time of 15 min, and under 800 psi of pressure. Dilution factors for ICP-OES are shown in Supplemental Table S2. Digested samples and cation standards were run in a matrix of 2% $HNO_3$ on a SpectroBlue ICP-OES in axial view mode (high sensitivity). Oxygen content was then calculated as the remaining mass not accounted for by combustion analysis or ICP-OES. Organic oxygen content was calculated with the assumption that $Na_2SO_4$ was the sole oxygen-containing inorganic species due to the lack of evidence for other molecular species present. $Na_2SO_4$ content was calculated based on the lower stoichiometric value of either sodium or sulfur content (e.g., if 2 mol sodium and 5 mol sulfur were present, 1 mol $Na_2SO_4$ would be used). Given the low concentrations of Ca, Mg, and K in all lignins (<0.06% for Ca, Mg, and K content summed) and biochar (<0.41% for Ca, Mg, and K content summed), this estimation represents the majority of inorganic oxygen present.

The chemical structure of all lignins and biochars was examined with Fourier-transform infrared spectroscopy (FTIR) and XRD, and biochar was additionally

characterized with Raman spectroscopy. FTIR measurements were performed on a ThermoFisher Nicolet iS50 FTIR spectrometer with a Smart iTX attuned total reflectance (ATR) accessory with a diamond crystal. Spectra were collected from wavenumbers of 600-4000 $cm^{-1}$, at a resolution of 4 $cm^{-1}$, with 64 scans per sample. XRD of all lignins and biochars was performed on a Bruker D8 Advance powder X-ray diffractometer with K$\alpha_{1,2}$ radiation, from 2$\theta$ values of 10-70°with a step size of 0.02°. Raman spectra were measured on a Horiba LabRam HR Evolution spectrometer with a 50× long-working distance objective and a frequency-doubled Nd:YAG laser (wavelength of 532 nm) at a power of 1 mW. Carbon D and G peaks were deconvoluted to determine $I_{dg}$ ratios, and XRD spectra were fit to determine graphitic crystallite sizes as previously described [31, 32].

Gel permeation chromatography (GPC) was employed to determine the number and weight average molar masses of the laboratory-isolated lignins, with acetylated samples utilized for the analysis [29]. An Agilent HPLC 1260 equipped with a Waters Styragel HR 4 (7.8 X 300 mm, Milford, MA, USA) column was used, with HPLC grade THF as the mobile phase with a 0.5 mL/min flow rate with UV detection at 280 nm and column temperature at 35 °C. As a reference, monodisperse polystyrene standards (Readycal, Fluka Analytical) were used in the range of 484 to 65,000 Da.

Lignin particle size was measured on a Malvern Mastersizer 2000 laser particle size analyzer with water as the dispersant and the assumption of non-spherical particles, as the biochar was ball milled. Before measurement, all samples except TCI alkaline and dealkaline lignins were placed in deionized water and sonicated

for 5 min to disperse lignin particles. TCI alkaline and dealkaline lignins were placed directly into the particle size analyzer to limit dissolution. Biochar and lignin morphology were examined on a Zeiss SUPRA 55VP field emission scanning electron microscope (SEM) with an electron high tension voltage of 20 kV and a working distance of approximately 8.2 mm.

Biochar electrical conductivity was measured on 100 mg of biochar with a compressive guard electrode setup, as described in previous work [33]. Direct current resistance measurements were taken on a Keithly 2540 Sourcemeter from the point of first contact between the electrode and the biochar, as determined by the sourcemeter reaching its lower current limit until no more pressure could be applied. Biochar packing fractions were calculated assuming a skeletal density of 2 g/cm$^3$ for all biochars.

Biochar surface area and pore size distribution were characterized with nitrogen sorption on a Micromeritics 3-Flex sorption analyzer 77 K for A95 biochar with and without $Na_2SO_4$. The Brunauer-Emmett-Teller (BET) model was used to determine surface area, and the non-local density functional theory carbon slit pore model was used to determine the pore size distribution. Gas sorption isotherms and pore size distributions are shown in Supplemental Figure S10.

### *2.5. Data analysis*

All statistical analyses were performed in Minitab (vers. 19.2020.1, Minitab LLC, State College, PA, USA), with a critical alpha set *a priori* to 0.05. Trends in shifts in the biochar elemental content with lignin elemental content were analyzed with linear regression, with lignin elemental content as the predictor variable

and biochar elemental content as the response variable. Impacts of lignin properties (H:C and O:C at. ratios, Na and S content, molecular weight, particle size, dominant monomer, and lignin thermal transitions) on biochar electrical conductivity or in-plane graphic crystallite size were analyzed with a forward selection regression model. The alpha value for inclusion in the model was set *a priori* to 0.25. The impacts of biochar treatments on biochar electrical conductivity were examined with analysis of variance (ANOVA), including particle size treatment (commercial, milled, or ground), washing to remove $Na_2SO_4$ (washed, as prepared, or hydrolysis), feedstock (commercial, poplar, or corn stover), or treatment type (hydrolysis, alkali, or commercial). Additionally, the impact of washing to remove $Na_2SO_4$ on alkali-poplar95 biochar electrical conductivity was examined with one-factor ANOVA.

## 3. Results and Discussion

### *3.1. Lignin characterization*

The lignins examined show a range of weight percentages of atomic species present (Figure 1). Carbon is the most abundant element in all lignins, ranging from 46.7 wt.% in TCI alkaline lignin to 61.7 wt.% in alkali-poplar150 lignin. Additionally, all lignins show oxygen (31.5-43.4 wt.%) and hydrogen (3.3-6.3 wt.%) content. Lignin inorganic content varies by isolation method. All commercial lignins (TCI alkaline, TCI dealkaline, Sigma alkali) and unwashed alkali lignins (alkali-poplar95) show the presence of sulfur (2.93-5.22 wt.%) and sodium (0.7-1.8 wt.%). In contrast, all other lignins show limited sulfur content (0-0.31

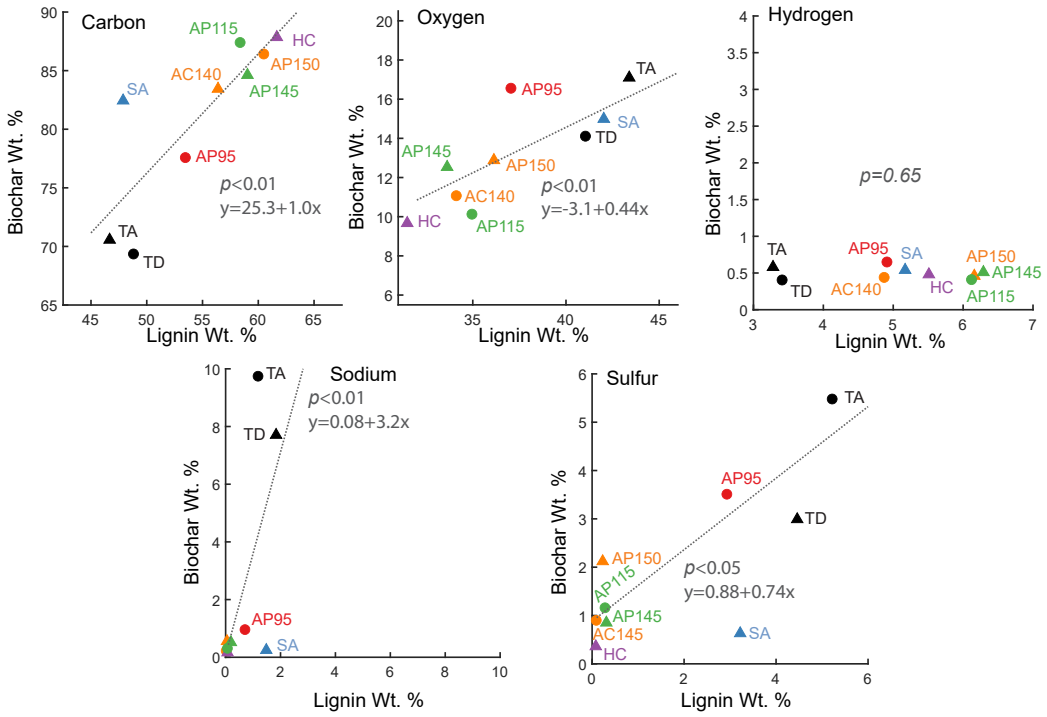


Figure 1: Comparison of weight % of C, H, O, Na, and S in all lignins before and after pyrolysis at 1100 °C. Linear regression trend lines are shown for all elements with a significant relationship ($p < 0.05$).

wt.%) and sodium content (0.02-0.19 wt.%). Magnesium, calcium, and potassium are present in limited quantities in all lignins (<0.1 wt. %).

As a result of the different methods used to reduce lignin particle size, lignins show a range of median particle sizes (8.36-375 $\mu$m) and particle size distributions (Supplemental Figure S1). The three commercial lignins (TCI alkaline, TCI deal-kaline, Sigma alkali) all show approximately 100 $\mu$m median particle sizes. All ball-milled lignins (alkali-poplar150, hydrolysis-corn, and alkali-corn140) show smaller particle sizes than other processing methods at 8-34 $\mu$m median particle size. Lignins that were ground with a pestle and mortar (alkali-poplar145, alkali-

poplar115, and alkali-poplar95) were found to have the largest median particle sizes between 160 and 375 $\mu$m. Ball-milled and commercial lignins show narrower particle size distributions than ground samples. This range of median particle sizes allows for the testing of particle size as a variable previously identified as a key factor impacting biochar electrical conductivity [33].

FTIR spectra were used to broadly categorize the lignins by their dominant monomer (Supplemental Figure S2a and full peak assignments given in Supplemental Table S5). TCI alkaline, TCI dealkaline, alkali-poplar95, 115, 145, and 150 and hydrolysis-corn lignins show a stronger response for peaks associated with syringyl monomers at 1113 $cm^{-1}$ (aromatic C-H in-plane deformation) and 1323 $cm^{-1}$ (C-O in syringyl ring), while Sigma-Aldrich alkali and alkali-corn140 lignins show a stronger response in peaks associated with guaiacyl monomers at 1032 $cm^{-1}$ (aromatic C-H in plane deformation) and 1263 $cm^{-1}$ (C-O in guaiacyl) [34]. Different lignin isolation procedures have limited impacts on monomer ratios. However, hydrolysis-corn shows a syringyl dominant spectra, while alkali-corn140 shows guaiacyl dominant spectra. Sigma-Aldirch alkali and alkali-corn140, which show stronger guaiacyl peaks, are isolated from spruce and corn, respectively, rather than the hardwood feedstocks used for the other lignins besides hydrolysis-corn [35, 36]. While the primary $Na_2SO_4$ peak (1112 $cm^{-1}$) overlaps with the primary syringyl peak, the presence of $Na_2SO_4$ can be identified by the secondary $SO_4$ peak at 627 $cm^{-1}$ [37], present as a strong peak in TCI alkaline, TCI dealkaline, alkali-poplar95, and alkali-poplar145 lignins, with weak peaks present in Sigma-Aldirch alkali, alkali-poplar115, and alkali-corn140

lignins. This finding is supported by the relative concentrations of Na in these lignins, with higher concentrations of Na present in TCI alkaline, TCI dealkaline, and alkali-poplar95 lignins than others. The presence of $Na_2SO_4$ in TCI dealkaline, alkali-poplar95, alkali-poplar115, and alkali-poplar145 is further supported by XRD patterns (Supplemental Figure S2b). Despite high levels of Na and S and FTIR peaks attributed to $SO_4$, TCI alkaline does not show a crystalline $Na_2SO_4$ response in XRD, indicating the presence of amorphous $Na_2SO_4$. The range of organic elemental composition, amount of $Na_2SO_4$ present, non-lignin contaminants, and dominant lignin monomers present in these lignins allow for the impact of these properties on the resulting biochar to be examined.

### *3.2. Lignin thermal transitions and biochar morphology*

DSC curves of lignin show two distinct patterns of behavior when heated (Supplemental Figure S3). The hydrolysis-corn lignin and washed alkali lignins (alkali-poplar145 and alkali-poplar115) show strong, broad glass transitions at 110 °C. In contrast, the commercial lignins (TCI alkaline, TCI dealkaline, and Sigma-aldrich alkali), alkali-corn140 and alkali-poplar150 show sharp, weak glass transitions at approximately 150 °C. Above this second glass transition, lignins that are high in $Na_2SO_4$ (as identified by elemental composition, FTIR, and XRD) show a sharp transition that is attributed to a polymorphic transition in $Na_2SO_4$ [38]. Finally, at high temperatures, a lignin softening transition is observed for all lignins [39, 40]. This transition begins at a lower temperature (118-200 °C) for hydrolysis lignins than for alkali or Kraft lignins (236-336 °C). In some lignins (alkali-poplar115, 145, and 150), the onset of thermal degradation

can be observed as noise in the DSC data above 300 °C.

The structure of the biochar post-pyrolysis varies as a result of these differences in thermal transitions (Figure 2). In biochar produced from the three commercial lignins (TCI alkaline, TCI dealkaline, and Sigma-Aldrich alkali), a powdered structure is observed, with particle sizes similar to the original lignins (Figure 2 and Supplemental Figure S1). In alkali-corn140 and hydrolysis-corn biochars, a clumped particle structure is observed (Figure 2). In contrast, in alkali-poplar95, alkali-poplar150, alkali-poplar115, and alkali-poplar145 biochars, a "carbon foam" structure is observed. Optical microscopy (Supplemental Figure S4) and SEM reveal that this "carbon foam" structure shows minimal distinction between individual particles (Figure 2), with small (<200 nm) clumped, primarily carbon "cobbling" observed via EDX and larger (1-2 $\mu$m), higher sodium content particles observed (Supplemental Figure S8). We hypothesize that this difference in behavior is related to thermal transitions in the lignin. In lignins with a powdered structure (TCI alkaline and dealkaline, Sigma-Aldrich alkali) or weakly clumped structure (hydrolysis-corn and alkali-corn140), DSC curves show weak or no glass transition. In contrast, lignins with a continuous, "carbon foam" structure (alkali-poplar150, 115, 145, and 95) all show strong glass transitions. Depending on the strength of these transitions, the structure of the resulting biochar shifts from a powder similar in size to the original lignins to a continuous material.

The formation of "carbon foam" structures could be attributed in part to the melting of $Na_2SO_4$. However, this behavior has previously been observed at pyrolysis temperatures as low as 300 °C, below the melting temperature of $Na_2SO_4$

[41]. Further, this behavior is not observed in the two highest $Na_2SO_4$ content biochars - TCI alkaline and dealkaline. Notably, all corn-derived lignins show clumped particle structures, all alkali-poplar lignins show "carbon foam" structures, and all commercial lignins have powdered structures. This finding indicates stronger softening transitions in poplar-derived lignins than corn-derived lignins prior to the formation of carbonized structures during pyrolysis. However, as previously observed [42], lignin melting behavior shows a significant relationship with molecular weight (p=0.002), with the highest molecular weight lignins (TA, TD, and SA Mw=28-60 kDa) showing no transition, moderate molecular weight lignins (HC and AC140, Mw=10-11.4 kDa) showing packed powder morphologies, and low molecular weight lignins, (AP95, 115, 145, 150 and AP95-Na, Mw=8-12.1 kDa) all showing continuous morphologies.

Notably, past studies have found that particle size may play an important role in the graphitization of lignin during pyrolysis [7, 10]. Based on the softening transitions observed and the resulting biochar morphology, we hypothesize that in lignins with a strong softening transition, particle size plays a limited role in resulting graphitization, as this size will have been lost before most pyrolysis reactions. Particle size does not appear to play a role in this transition, as similar lignins with large differences in size (such as alkali-poplar115 at 19 $\mu$m and alkali-poplar145 at 375 $\mu$m) have these same thermal transitions and form similar structures. However, particle size may still play a role in the pyrolysis of lignins with a weak softening transition (such as Sigma-Aldrich alkali and TCI alkaline and dealkaline lignins).

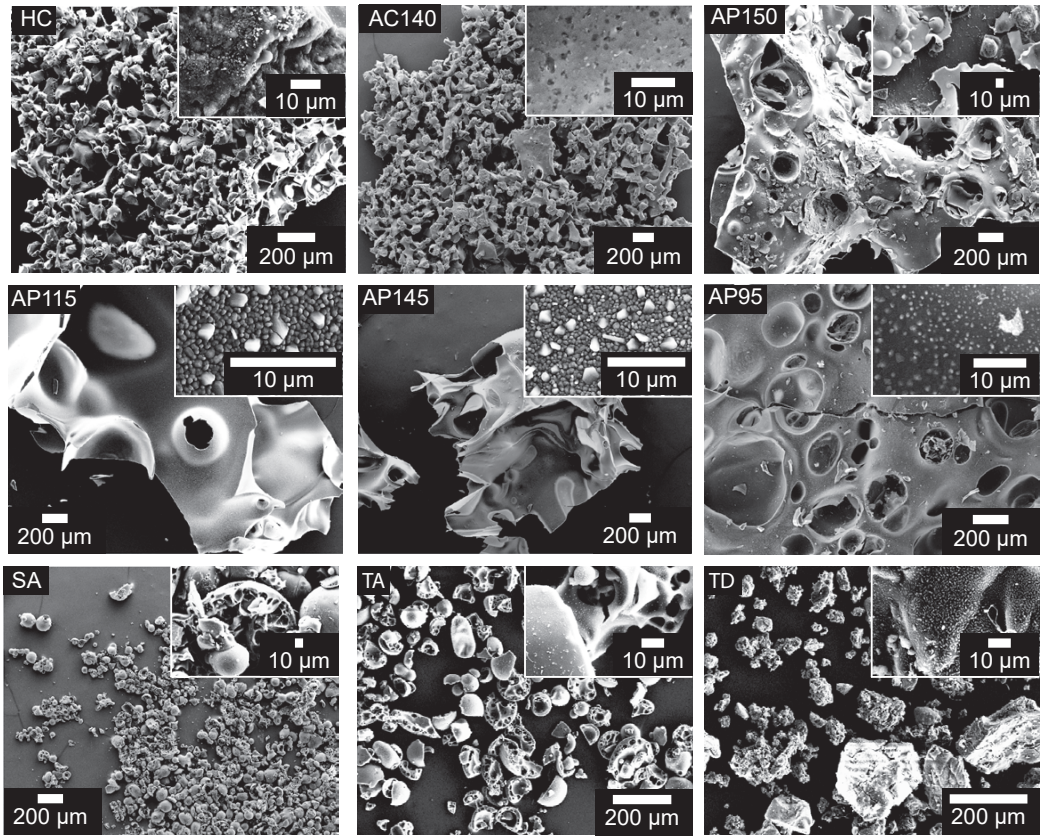


Figure 2: SEM micrographs of biochars produced from all lignins. Main images are at 50-250× magnification to highlight particle geometry, while insets are at 1000-3000× magnification to highlight surface features.

### *3.3. Biochar characterization*

Biochar yield varied between 21 and 45 wt.%, depending on lignin feedstock (Figure 3a). Typically, lignins with higher sodium content (TCI alkaline, TCI dealkaline, Sigma-Aldrich alkali, and Alkali-poplar95) resulted in higher biochar yields, which is attributed to the lack of reaction of $Na_2SO_4$ during pyrolysis. In biochar that formed a carbon foam structure, the biochar had expanded out of the alumina boat used. Therefore, some biochar was lost during pyrolysis. The reac-

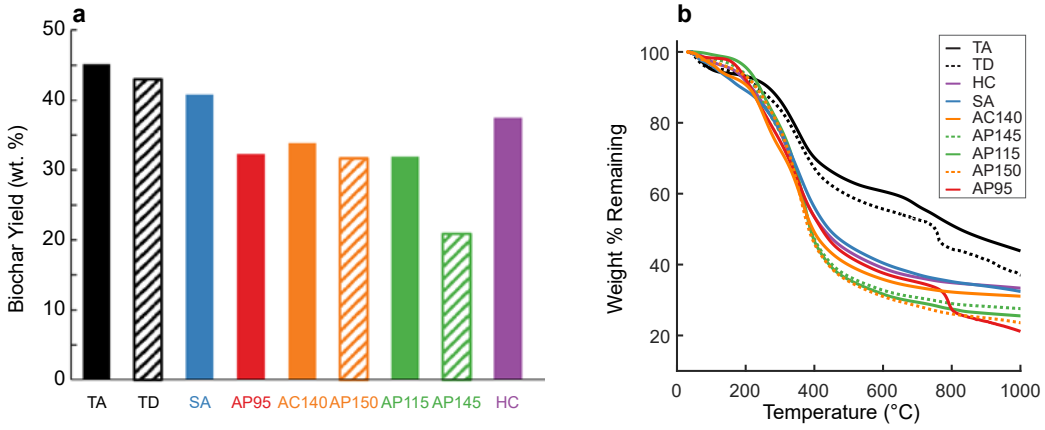


Figure 3: (a) Pyrolysis yield for each lignin. (b) TGA curves for each lignin under heating rates replicating tube furnace pyrolysis. Legend order shows the weight percent remaining at 1000 °C from highest to lowest.

tions that were responsible for these pyrolysis yields were examined with TGA, and final masses at 1000 °C generally agreed with trends in biochar production yields (Figure 3b). At low temperatures (30-110 °C), all lignins show small mass losses (0.9-5.3%) associated with moisture evaporation. At high temperatures, two distinct pyrolysis behaviors are observed - with the TCI alkaline and dealkaline lignins and the alkali-poplar95 lignins all showing degradation in the 600-800 °C region.

In contrast, other lignins show only minor mass loss in this region. This mass loss has previously been associated with the degradation of ether linkages into CO and $CO_2$ [43]. Additionally, these three lignins are some of the highest in sodium and sulfur content (Figure 1), and decomposition of $Na_2SO_4$ has previously been observed at around 850 °C in the presence of carbon [44]. Additionally, the presence of alkali metals, such as sodium, has previously been observed to catalyze

the decomposition of biomass during pyrolysis, which could be responsible for the presence of this mass loss in high $Na_2SO_4$ lignins [25].

The carbon, oxygen, sodium, and sulfur content in the biochar is found to be significantly impacted by the concentration of that element present in lignin ($p < 0.05$, Figure 1). Carbon content shows a consistent increase of approximately 25 wt.% with pyrolysis, attributed to loss of oxygen and hydrogen with pyrolysis. As a result of this shift, biochar carbon content is additive to starting lignin carbon content (e.g., lignin that started at 50% C results in approximately 75% C biochar). Only SA shows a meaningful variation from this trend, gaining approximately 35 wt.% carbon. Due to limited evidence for the presence of carbon-containing inorganic compounds, this carbon is assumed to be entirely organic. We note that some inorganic species, such as Ca, were found via ICP-OES, which would commonly be present in biomass as carbon-containing species (e.g., $CaCO_3$), which could indicate the presence of some inorganic carbon [16], but also could be present as CaO or $CaSO_4$ following thermal decomposition of $CaCO_3$.

Similarly, biochar oxygen content increases with increasing lignin oxygen content, however, at a slower rate than carbon, with approximately 44% of the lignin oxygen remaining after pyrolysis on average. Biochar organic oxygen content is expected to play an important role in biochar electrical conductivity [10, 20]. Lignin hydrogen content was not found to have a significant impact on biochar hydrogen content ($p = 0.65$). All biochars showed hydrogen content of approximately 0.5 wt.%, while lignin hydrogen content varied from 3.3-6.3 wt.%.

This similar hydrogen content indicates that in these biochars, H:C atomic ratios, and therefore inferred graphitic structure diameters [45], are driven primarily by carbon content. Biochar and lignin atomic compositions are tabulated in Supplemental Tables S3 and S4.

All biochars showed low (<0.2 wt.%) Mg, Ca, and K concentrations (Supplemental Table S4). In contrast, biochars from acidification processes without washing steps (TCI alkaline and dealkaline, alkali-poplar95, and Sigma-Aldrich alkali) show high concentrations of Na and S. These concentrations are found to be typically significantly higher than the concentration of sodium or sulfur in the lignin feedstock ($p < 0.01$ and $< 0.05$ for Na and S, respectively). In the case of sodium, this increase in concentration (3.2×) roughly matches the change in mass (average yield of 35%, Figure 3), indicating that minimal sodium has reacted off during pyrolysis. Molar ratios of sodium to sulfur in biochar show differing shifts depending on the lignin feedstock, which indicates the presence of multiple sodium and sulfur-containing compounds or organic sulfur. However, XRD and FTIR spectra of both lignin and biochar show $Na_2SO_4$ as the predominant form of both sodium and sulfur in all biochar. A meaningful portion of biochar and lignin oxygen is inorganic, with between 3 and 35% of total oxygen present in $Na_2SO_4$ based on sodium content (Supplemental Table S4).

Sigmoidal electrical percolation behavior is observed in all biochars as they are compressed (Figure 4b). At low compressions, all biochars show highly resistive behavior, as the non-conductive air dominates the unpacked powder. At a packing fraction of approximately 0.25, the percolation threshold is reached,

and electrical conductivity rapidly increases. The percolation threshold is similar for all biochars, indicating similar particle geometry and packing despite differences in the structure after pyrolysis but before ball milling. The peak electrical conductivity of all biochars varied by two orders of magnitude between biochars, from 0.19 S/cm for TCI alkaline biochar to 18.9 S/cm for alkali-poplar95 biochar. These variations are consistent with what has previously been observed for pyrolysis of lignin at 1100 °C with electrical conductivity measured with the same method and in the middle of a range of values previously observed for all lignin-derived biochars [10]. The upper range (>10 S/cm) of these conductivities are comparable to those of electrically conductive carbon blacks [33, 46], and are sufficient for many electrical applications, including anti-static materials, sensors, and conductive additives in batteries. At a pyrolysis temperature of 1100 °C, no further increase in electrical conductivity is expected with further increases in pyrolysis temperature [21].

A number of factors impact biochar electrical conductivity: the size of graphitic crystallites, displacements and deformations on those crystallites, biochar surface groups, and biochar particle size [10, 20, 21]. XRD patterns of the biochar show variation in the in-plane size of graphitic crystallites ($L_a$) but minimal shifts in size or distance between sheets in the stacking direction ($L_c$ and $d_{002}$) with an average and standard deviation of $1.2 \pm 0.1$ graphene planes per crystallite across all samples. The in-plane size of graphitic crystallites varies from 3.4 Å for TCI dealkaline biochar to 41 Å for alkali-poplar115-biochar. TCI alkaline and dealkaline biochar show poor fits of XRD patterns relative to other biochar, which

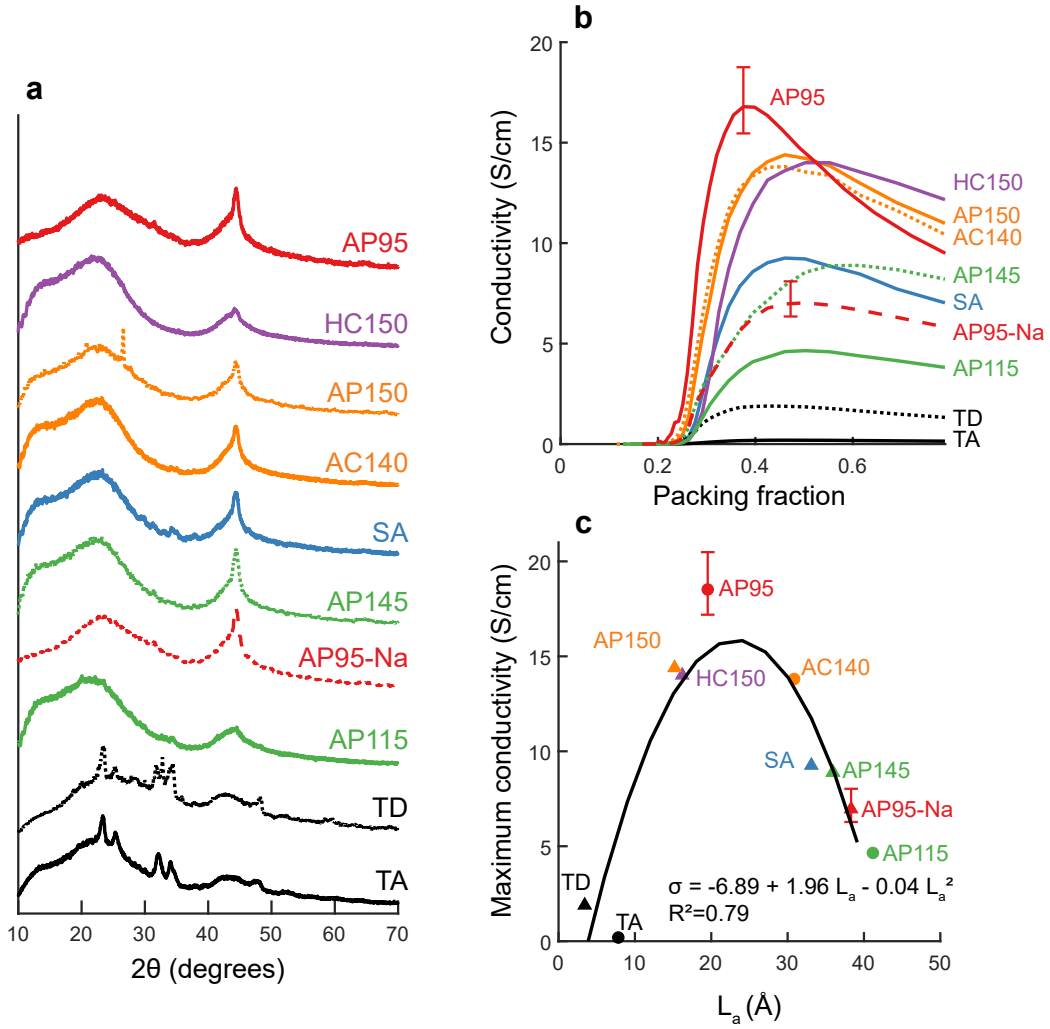


Figure 4: Characterization of biochar graphitic structure and electrical conductivity showing (a) XRD patterns. Lines are stacked in order of maximum electrical conductivity from highest (top) to lowest (bottom), (b) electrical conductivity as a function of packing fraction, and (c) relationship between in-plane graphitic crystallite size and electrical conductivity. Error bars in (b) and (c) represent the maximum and minimum values of peak conductivity for three samples from a comparison of AP95 with and without $Na_2SO_4$, and the point or line represents the median value.

400 is attributed to the high contribution of inorganic components to the XRD pattern

401 in these biochars, which were not included in the fitting procedure (Supplemental

Table 2: Calculated XRD (in-plane graphitic crystallite size ($L_a$), out-of-plane graphitic crystallite size ($L_c$), crystallite aspect ratio ($L_a/L_c$), and space between planes (d) and Raman values (Intensity ratio of fit d peak go g peak $I_{DG}$ and width of G peak ($W_G$)) and peak electrical conductivity for all biochar. Complete Raman spectra are given in Supplemental Figure S5, and XRD fits are given in Supplemental Figure S6.

| | $L_a$( Å) | $L_c$ (Å) | $L_a/L_c$ | d (Å) | $I_{DG}$ | $W_G$ | Conductivity (S/cm) |
|---|---|---|---|---|---|---|---|
| TCI alkaline | 7.8 | 4.6 | 1.7 | 4.0 | 1.1 | 148.0 | 0.2 |
| TCI dealkaline | 3.4 | 5.2 | 0.7 | 3.7 | 1.1 | 133.9 | 1.9 |
| Sigma-Aldrich alkali | 33.1 | 5.0 | 6.6 | 4.1 | 1.1 | 151.2 | 9.3 |
| Hydrolysis-corn | 16.2 | 4.9 | 3.3 | 4.1 | 1.2 | 147.7 | 14.0 |
| Alkali-corn140 | 15.2 | 4.3 | 3.5 | 4.4 | 1.1 | 153.9 | 14.4 |
| Alkali-poplar150 | 30.9 | 4.6 | 6.7 | 4.3 | 1.1 | 137.5 | 13.8 |
| Alkali-poplar115 | 41.2 | 4.9 | 8.4 | 4.2 | 1.0 | 146.8 | 4.6 |
| Alkali-poplar145 | 35.9 | 4.9 | 7.3 | 4.3 | 1.1 | 146.0 | 8.9 |
| Alkali-poplar95 | 19.5 | 5.1 | 3.8 | 4.4 | 1.2 | 146.1 | 18.5 |
| Alkali-poplar95-Na | 38.3 | 4.0 | 9.5 | 3.8 | | | 7.0 |

Figure S6a and b). Minimal shifts are observed in Raman spectra between samples (Supplemental Figure S5). All biochars show the typical D and G peaks that are typical for non-graphitizing carbons [31]. The intensity ratio of these peaks ($I_{dg}$) ranges from 1.03-1.18. In TA, an additional peak is observed at 1058 $cm^{-1}$, which is attributed to $Na_2SO_4$ (Supplemental Figure S5) [47]. TCI alkaline and dealkaline biochars have a shallower valley between the D and G peaks than other biochars. The ratio of this valley depth to the height of the G-peak has previously been correlated with the degree of graphitization [48]. Combined with limited $10l$ peaks in the XRD patterns of TCI alkaline and dealkaline biochars and low electrical conductivity, this finding demonstrates that these biochars have lower graphitization than the other biochars examined. A full summary of fit values from XRD and Raman is given in Table 2.

Despite the range of properties and electrical conductivity identified herein,

no statistically significant relationship was found with a linear regression between any of the examined lignin properties (H:C and O:C at. ratios, Na and S wt. %, molecular weight, particle size, dominant monomer, and lignin thermal transitions) and biochar electrical conductivity ($p > 0.05$ for all, Figure 5). Similarly, one-factor ANOVAs found no statistically significant differences ($p > 0.05$ for all) between treatment groups, including particle size treatment (commercial, milled, or ground), washing to remove $Na_2SO_4$ (washed, as prepared or received, or hydrolysis), feedstock (commercial, poplar, or corn stover), or treatment type (hydrolysis, alkali, or commercial). This lack of significance holds even when processing methods and feedstock for commercial lignins are ungrouped, and feedstock is assumed to be mixed wood for TCI alkaline and dealkaline lignin, softwood for Sigma-Aldrich alkali lignin, and treatment type is assumed to be alkaline for TCI alkaline and dealkaline lignin and alkali for Sigma-Aldrich alkali lignin.

However, when examining the relationship between lignin properties and biochar in-plane graphitic crystallite size ($L_a$, Supplemental Figure S8)), a significant relationship was observed with lignin H:C atomic ratio ($p = 0.042$). This relationship shows an increasing graphitic crystallite size with an increasing H:C ratio. Notably, despite a wide range of hydrogen content in the lignin feedstocks, the biochar produced shows limited variation in hydrogen content (Figure 1). This finding indicates that feedstock hydrogen content has a limited effect on the final molecular structure. Instead, hydrogen plays a role in the pyrolysis reactions that lead to the formation of those structures. This finding is consistent with past mod-

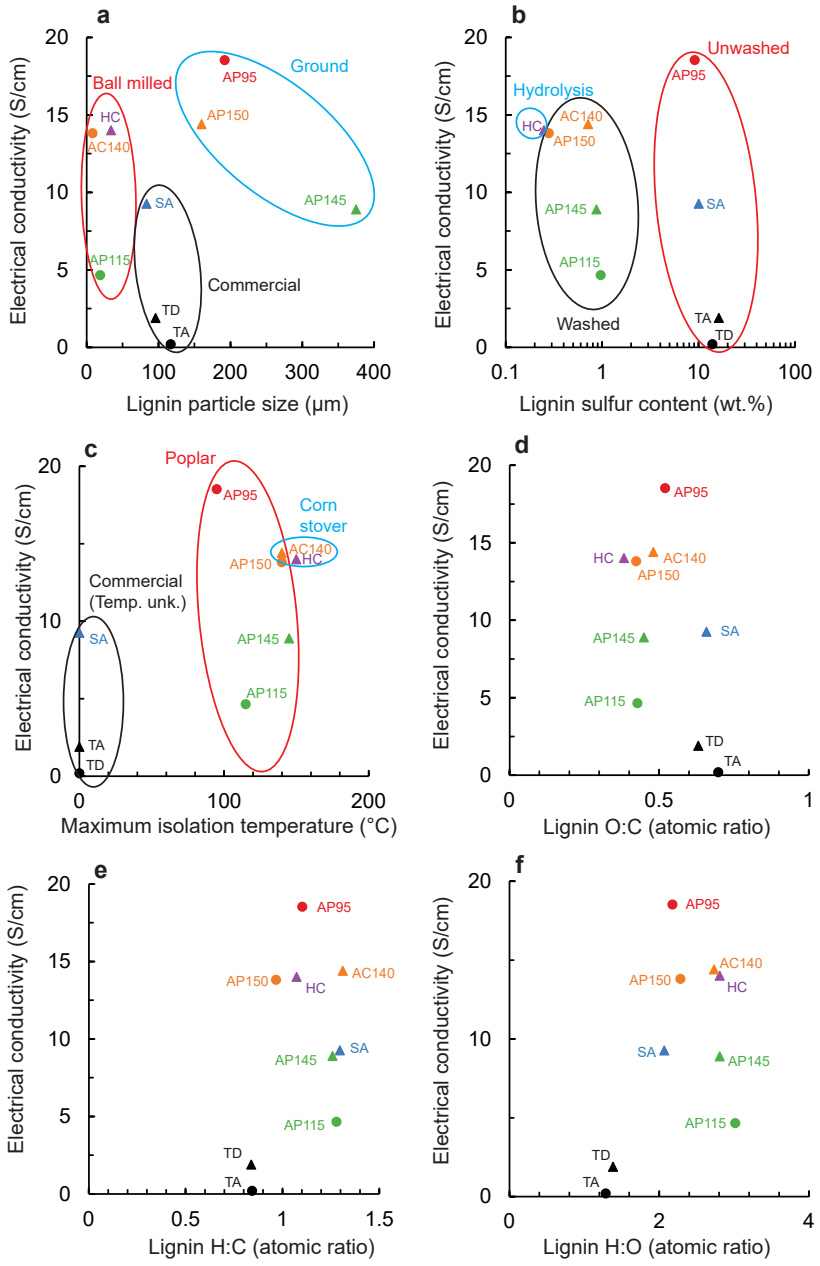


Figure 5: Comparison of biochar electrical conductivity with (a) lignin particle size, (b) lignin sulfur content, (c) lignin max. isolation temperature, (d) lignin organic O:C ratio, (e) lignin H:C ratio, and (d) lignin organic H:O ratio. Labeled groups are treatment groups.

els of biomass pyrolysis, which state that when insufficient hydrogen is present in a feedstock to react with oxygen, which forms distortions in the graphitic structure, these distortions persist, even at high pyrolysis temperatures, limiting the possible degree of graphitization of the feedstock [20]. As oxygen content shows lower variation between lignin feedstocks (O:C ratios of 0.38-0.70, relative to H:C ratios of 0.84-1.31), the hydrogen content is the primary driver of variation in graphitization of the lignin feedstocks examined. Future work examining a wider range of lignin oxygen content could better highlight the role of oxygen in these reactions. As a result, it may be preferable to produce lignin with higher guaiacyl monomer content (H:O at. ratio of 4) rather than syringyl dominant lignin (H:O at. ratio of 3.3). We note, however, that no relationship is observed between the biochar H:O ratio or in-plane graphitic crystallite size and the dominant monomer in this work, and relatively few guaiacyl-dominant lignins (AC140 and SA) were examined. Further, those two lignins show relatively small differences in electrical conductivity, both within the upper half of electrical conductivities examined (14.4 and 9.3 S/cm for AC140 and SA, respectively).

Alkali-poplar95 biochar, as the highest electrical conductivity biochar, was selected for further testing to examine the impact of inherent $Na_2SO_4$ on lignin-derived biochar electrical conductivity and carbon structure. After washing to remove $Na_2SO_4$ from alkali-poplar95 (alkali-poplar95-Na), limited sulfur or sodium content was observed via EDX, and no $Na_2SO_4$ peaks were observed via XRD (Supplemental Figure S9). An ANOVA assessing the impact of $Na_2SO_4$ removal treatment on alkali-poplar95 biochar electrical resistivity found a statistically sig-

nificant impact from $Na_2SO_4$ treatment ($p < 0.01$). Alkali-poplar95 biochar had an average electrical conductivity of 17 ± 1.6 S/cm (Figure 4 and Supplemental Figure S9). With $Na_2SO_4$ removed, electrical conductivity was reduced to 7.0±0.5 S/cm.

The mechanisms behind this difference in electrical conductivity were further explored with XRD, finding a meaningful increase in crystallite size of the graphitic 10 plane ($L_a$) with the removal of $Na_2SO_4$ (Figure 4a and Table 2). Alkali-poplar95 biochar shows an in-plane crystallite size of 16.2 Å on average. With the removal of $Na_2SO_4$, in-plane crystallite size meaningfully increases to 38.3 Å. In contrast, crystallite size in the stacking 002 direction ($L_c$) only shows minor shifts between 4-5 Å for both treatments with a distance of approximately 4 Å between each layer. Importantly, this finding indicates that the presence of $Na_2SO_4$ inhibits graphitization in lignin-derived biochars. Further, the BET surface area of the biochar decreases from 27.10 $m^2$/g in alkali-poplar95 with $Na_2SO_4$ to 8.16 $m^2$/g when $Na_2SO_4$ is removed. This decrease in surface area with $Na_2SO_4$ removal is driven by a decrease in pores with a width of less than 35 Å (Supplemental Figure S10b). The combination of increased graphitic crystallite size and decreased BET surface area of smaller pores is consistent with past findings of micro-pore closure with increasing graphitization [49]. This is further supported by increased hysteresis during desorption in akali-poplar95 relative to with $Na_2SO_4$ removed, indicating the presence of constricted pores when $Na_2SO_4$ is present, that are closed when $Na_2SO_4$ is not present [49].

Beyond alkali-poplar95 with and without $Na_2SO_4$ removal, individual com-

parisons can be made based on similar lignins with individual differences in processing. Alkali-poplar150 and alkali-corn140 were processed similarly, but different feedstocks (poplar and corn stover) and particle sizes (34 $\mu$m and 160 $\mu$m), but the resulting biochars have similar electrical conductivities (13.8 and 14.4 S/cm). However, they have different graphitic crystallite sizes with an in-plane graphitic crystallite size of 15.2 and 30.9 Å for corn and poplar, respectively. Alkali-poplar95, which was processed similarly to alkali-poplar150 but with a lower treatment temperature and no washing to remove $Na_2SO_4$, resulted in higher electrical conductivity. Similarly, alkali-poplar115 and alkali-poplar145 have similar processing, chemical content, and graphitic crystallite size with differences in treatment temperature, but alkali-poplar145 shows higher electrical conductivity than alkali-poplar115. The two corn-stover-derived lignins examined (hydrolysis-corn and alkali-corn140) show broadly similar properties despite the different processing methods used; as alkali-corn140 was washed to remove $Na_2SO_4$, both have low sodium and sulfur content, and both lignins were ball milled and therefore show similar particle sizes. When alkali-poplar95 is washed to remove $Na_2SO_4$, the electrical conductivity decreases, and the in-plane graphitic crystallite size increases to be comparable to alkali-poplar115 and alkali-poplar145. These two lignins were processed similarly to alkali-poplar95, except they were washed to remove $Na_2SO_4$, indicating that this washing step drives the large differences between these three otherwise similar lignins.

As biochar graphitic crystallite size only meaningfully varies in the in-plane direction, the aspect ratio of graphitic crystallites varies greatly between differ-

ent biochars. This shift in graphitic crystallite size is found to play a key role in biochar electrical conductivity. A strong quadratic relationship is found between in-plane graphitic crystallite size and biochar conductivity ($p < 0.01$, Figure 4c). This relationship peaks in electrical conductivity at an in-plane graphitic crystallite size of 23 Å. We propose two mechanisms for this behavior, which expand on the previously developed quasi-percolation model for biochar electrical conductivity [21, 30]. At small in-plane graphitic crystallite sizes, such as are found in TCI alkaline and dealkaline biochar, limited graphitization has occurred due to the presence of high quantities of $Na_2SO_4$ as indicated by elemental composition, XRD, and Raman spectroscopy. Graphitic crystallites in these materials have limited electrically conductive contact between crystallites and are separated by lower electrical conductivity displaced graphitic carbon, as predicted by previous quasi-percolation models [21]. As the size of these crystallites expands, such as in alkali-corn-140 and hydrolysis-corn biochar, there are increased contacts between electrically conductive regions. These contacts reach a maximum at in-plane graphitic crystallite sizes of approximately 23 Å, corresponding to a graphitic crystallite aspect ratio of 3.8 $L_a/L_c$. Above this contact, the high aspect ratio and the random orientation of graphitic crystallites [50] limit contacts between the crystallites, resulting in lower electrical conductivity. This proposed behavior matches those previously observed for percolation in packed powder systems, where higher aspect ratios result in reduced electrical conductivity [46]. In addition, the graphitic crystallite size that results in the highest biochar electrical conductivity is similar to that of highly electrically conductive carbon blacks [11].

This similarity suggests that similar mechanisms for crystallite packing occur in petroleum-derived carbon black.

A complex series of multi-phase reactions is observed during pyrolysis, driven by the melting behavior of some lignins at low temperatures, melting of $Na_2SO_4$ at high temperatures, and secondary reactions of liquid oil and tar pyrolysis products back to solid biochar. No statistically significant trends were observed in electrical conductivity or graphitic crystallite size based on the melting behavior of the biochar. However, this may in part be due to the compounding of other effects, as two of the lignins with no observed melting behavior (TA and TD) were also the highest in $Na_2SO_4$, and the two lignins that showed clumped-powder behavior (HC and AC140) were the lowest in $Na_2SO_4$ content, while continuous morphologies showed a range of $Na_2SO_4$ content. Further, at 1000 °C, lignins that showed no melting behavior showed the highest yields at 200-1000 °C via both TGA and pyrolysis yields at 1100 °C (Figure 3), followed by clumped powder morphologies, with continuous morphologies having the lowest yields. While previous studies have observed increased decomposition at low pyrolysis temperatures in lignins that show melt behavior [42], an alternative explanation is that non-melting lignins have a higher molecular weight, which is also correlated with increased biochar yields, rather than the melting itself. Further, at present, it is unknown how these shifts in low-temperature behavior impact the formation of graphitic structures at pyrolysis temperatures above 900 °C. Critical examination of this phenomenon, controlling for the identified compounding factors herein, could provide additional insight into which lignin isolation procedures and lignin

properties provide the best feedstock for differing carbon applications.

Multiple structures of $Na_2SO_4$ were observed via SEM-EDX, with $Na_2SO_4$ being present as both a "skin" on the outside of the biochar and integrated as approximately 1 $\mu$m structure between the majority carbon structures (Supplemental Figure S8). The impacts of $Na_2SO_4$ melting on lignin pyrolysis, as well as the mechanisms responsible for the herein observed shifts in carbon structure with $Na_2SO_4$ presence, is a particularly interesting area for further study. A better understanding of these mechanisms would allow for the carbon structures of lignin-derived carbons to be better optimized for specific applications. Past work on molten salt interactions during pyrolysis has shown molten salt to impact carbon structures [51, 52], and a better understanding of these interactions in lignin pyrolysis is needed to modify the structures of lignin-derived carbons to specific applications.

This study highlights the development of low aspect ratio graphitic crystallites but well-graphitized carbon structures as a potential method to increase the electrical conductivity of carbons produced from non-graphitizing feedstocks. Future work should examine if biochar could be produced with limited disordered and displaced graphitic content but with graphitic crystallite aspect ratios approaching 1, as higher electrical conductivities of the bulk material may be possible. Importantly, this work demonstrates that $Na_2SO_4$ levels in lignin can be controlled to selectively control graphitization of lignin-derived biochar and tune graphitic crystallite size and electrical conductivity to a desired application. Modification of pore size distributions and surface area via selective $Na_2SO_4$ removal can

tune these critical factors for carbon applications such as battery active materials [53]. Further, in future work, multiple variables, such as pyrolysis temperature and $Na_2SO_4$ level, could be tuned to examine combinations that maximize highly electrically conductive carbon production while minimizing energy consumption during production. Given the strong performance previously demonstrated by lignin-derived carbons across multiple applications [7, 11, 14, 15], this work provides key guidance on feedstock selection and modification to meet the requirements of carbons as commercial application of lignin-derived carbons continues to grow. However, the additional processing step required to remove $Na_2SO_4$ would be expected to introduce additional costs, and the benefits of additional tuning of the carbon properties should be carefully evaluated against these costs. Process considerations, such as tuning the amount of NaOH added during delignification and the sulfuric acid addition during precipitation of alkali lignins or selection of sulfur-free processes (e.g., hydrolysis), could allow for tuning the sodium sulfate content of lignin to a desired carbon application without additional washing steps. However, these process changes would need to be carefully evaluated against the outputs of the biorefinery process as a whole. The simple water washing method demonstrated herein would be expected to be lower cost compared to other methods to tune biomass-derived carbon properties such as iron catalysts, which must be removed with acid washes [15] or activation processes that consume more costly activation agents, such as KOH [14].

## 4. Conclusions

This work highlights that all lignins are not equal for producing electrically conductive biochar, with a 100-fold difference in electrical conductivity between the most and least conductive biochar measured. The wide range of electrical conductivities observed herein for lignin-derived biochars confirms that similar ranges observed between past studies are not exclusively due to differences in biochar production or electrical conductivity measurement methods. $Na_2SO_4$ content in lignin is identified as a significant factor in lignin-derived biochar carbon structure, with $Na_2SO_4$ inhibiting the formation of larger graphitic crystallites. However, the aspect ratio of graphitic crystallites in lignin-derived biochar plays an important role in the electrical conductivity of the resulting biochar, with a quadratic relationship observed with a maximum electrical conductivity at an aspect ratio of $\sim$ 4. Many of the examined lignin-derived biochars have higher aspect ratios, resulting in lower electrical conductivity despite larger graphitic crystallites. Therefore, the presence of moderate amounts of $Na_2SO_4$ can be used to selectively tune the carbon structure in lignin-derived carbons and maximize electrical conductivity. This finding builds on past quasi-percolation models that describe the packing of graphitic crystallites within carbon particles as an important contributor to their bulk electrical conductivity and can help to inform the development of future electrically conductive, non-graphitizing carbons.

## Supplementary material

Supplementary material to this article is openly available at https://doi.org/10.1016/j.jaap.2024.106600

## Acknowledgements

We would like to thank Dr. Nicholas P. Stadie and Dalton Compton for their assistance with gas sorption measurements. S.K.'s contribution was funded in part through a Ph.D. Fellowship from the Environmental Research and Education Foundation. This work was performed in part at the Montana Nanotechnology Facility, a member of the National Nanotechnology Coordinated Infrastructure (NNCI), which is supported by the National Science Foundation (Grant #ECCS-1542210). D.B.H., B.S., V.E.B., and D.N.D.'s contribution was based upon work supported by the U.S. Department of Energy's Office of Energy Efficiency and Renewable Energy (EERE) under the Bioenergy Technologies Office Award # DE-EE0008148. This work represents the views of the authors, not necessarily those of the funders.

## References

[1] Maria-Magdalena Titirici, Robin J. White, Nicolas Brun, Vitaliy L. Budarin, Dang Sheng Su, Francisco del Monte, James H. Clark, and Mark J. MacLachlan. Sustainable carbon materials. *Chem. Soc. Rev.*, 44:250–290, 2015. doi: 10.1039/C4CS00232F.

[2] Sabornie Chatterjee and Tomonori Saito. Lignin-derived advanced carbon materials. *ChemSusChem*, 8:3941–3958, 12 2015. ISSN 1864-564X. doi: 10.1002/CSSC.201500692.

[3] D. S. Bajwa, G. Pourhashem, A. H. Ullah, and S. G. Bajwa. A concise review of current lignin production, applications, products and their environmental impact. *Industrial Crops and Products*, 139:111526, 11 2019. ISSN 0926-6690. doi: 10.1016/J.INDCROP.2019.111526.

[4] Jason K. Hansen, Jacob J. Jacobson, Kara G. Cafferty, Patrick Lamers, and Mohammad S. Roni. Quantifying supply risk at a cellulosic biorefinery. *33rd International Conference of the System Dynamics Society*, 7 2015. URL `https://www.osti.gov/biblio/1357903`.

[5] Julia Wenger, Verena Haas, and Tobias Stern. Why can we make anything from lignin except money? towards a broader economic perspective in lignin research. *Current Forestry Reports*, 6:294–308, 12 2020. ISSN 21986436. doi: 10.1007/S40725-020-00126-3.

[6] Richard J. A. Gosselink. *Lignin as a Renewable Aromatic Resource for the Chemical Industry*. PhD thesis, Wageningen University, 2011. URL `https://www.proquest.com/dissertations-theses/lignin-as-renewable-aromatic-resource-chemical/docview/2568538894/se-2?accountid=28148`.

[7] William J. Sagues, Ankush Jain, Dylan Brown, Salonika Aggarwal, Antonio

Suarez, Matthew Kollman, Seonghyun Park, and Dimitris S. Argyropoulos. Are lignin-derived carbon fibers graphitic enough? *Green Chemistry*, 21: 4253–4265, 8 2019. ISSN 14639270. doi: 10.1039/C9GC01806A.

[8] Muhannad Al Aiti, Dieter Jehnichen, Dieter Fischer, Harald Brünig, and Gert Heinrich. On the morphology and structure formation of carbon fibers from polymer precursor systems. *Progress in Materials Science*, 98:477–551, 10 2018. ISSN 0079-6425. doi: 10.1016/J.PMATSCI.2018.07.004.

[9] Xiaoyu Wu, Junhua Jiang, Chongmin Wang, Jian Liu, Yunqiao Pu, Arthur Ragauskas, Songmei Li, and Bin Yang. Lignin-derived electrochemical energy materials and systems. *Biofuels, Bioproducts and Biorefining*, 14:650–672, 5 2020. ISSN 1932-1031. doi: 10.1002/BBB.2083.

[10] Seth Kane, Rachel Ulrich, Abigail Harrington, Nicholas P. Stadie, and Cecily Ryan. Physical and chemical mechanisms that influence the electrical conductivity of lignin-derived biochar. *Carbon Trends*, page 100088, 2021. ISSN 2667-0569. doi: 10.1016/j.cartre.2021.100088.

[11] Seth Kane, Aksiin Storer, Wei Xu, Cecily Ryan, and Nicholas P. Stadie. Biochar as a renewable substitute for carbon black in lithium-ion battery electrodes. *ACS Sustainable Chemistry & Engineering*, 10(37):12226–12233, 2022. doi: 10.1021/acssuschemeng.2c02974.

[12] Haiping Yang, Rong Yan, Hanping Chen, Dong Ho Lee, and Chuguang Zheng. Characteristics of hemicellulose, cellulose and lignin pyroly-

679 sis. *Fuel*, 86:1781–1788, 8 2007. ISSN 0016-2361. doi: 10.1016/
680 J.FUEL.2006.12.013.

681 [13] Michael R Snowdon, Amar K Mohanty, and Manjusri Misra. A study of car-
682 bonized lignin as an alternative to carbon black. *ACS Sustainable Chemistry*
683 *& Engineering*, 2:1257–1263, 2014. doi: 10.1021/sc500086v.

684 [14] Kai Chen, Zi-Jing He, Zhi-Hua Liu, Arthur J. Ragauskas, Bing-Zhi Li,
685 and Ying-Jin Yuan. Emerging Modification Technologies of Lignin-based
686 Activated Carbon toward Advanced Applications. *ChemSusChem*, 15(21):
687 e202201284, 2022. ISSN 1864-564X. doi: 10.1002/cssc.202201284.

688 [15] William J. Sagues, Junghoon Yang, Nicholas Monroe, Sang-Don Han, Todd
689 Vinzant, Matthew Yung, Hasan Jameel, Mark Nimlos, and Sunkyu Park.
690 A simple method for producing bio-based anode materials for lithium-ion
691 batteries. *Green Chemistry*, 22:7093–7108, 10 2020. ISSN 1463-9270. doi:
692 10.1039/D0GC02286A.

693 [16] Nancy Chen and Srikanth Pilla. A comprehensive review on transforming
694 lignocellulosic materials into biocarbon and its utilization for composites
695 applications. *Composites Part C: Open Access*, 7:100225, 3 2022. ISSN
696 2666-6820. doi: 10.1016/J.JCOMC.2021.100225.

697 [17] Wenli Zhang, Xueqing Qiu, Caiwei Wang, Lei Zhong, Fangbao Fu, Jiahao
698 Zhu, Zejie Zhang, Yanlin Qin, Dongjie Yang, and Chunbao Charles Xu.
699 Lignin derived carbon materials: current status and future trends. *Carbon*

*Research*, 1(1):14, July 2022. ISSN 2731-6696. doi: 10.1007/s44246-022-00009-1.

[18] Amar K. Mohanty, Singaravelu Vivekanandhan, Oisik Das, Lina M. Romero Millán, Naomi B. Klinghoffer, Ange Nzihou, and Manjusri Misra. Biocarbon materials. *Nature Reviews Methods Primers*, 4(1):1–21, March 2024. ISSN 2662-8449. doi: 10.1038/s43586-024-00297-4.

[19] Janea Köhnke, Harald Rennhofer, Helga Lichtenegger, Arunjunai Raj Mahendran, Christoph Unterweger, Batirtze Prats-Mateu, Notburga Gierlinger, Elisabeth Schwaiger, Arnulf Kai Mahler, Antje Potthast, and Wolfgang Gindl-Altmutter. Electrically conducting carbon microparticles by direct carbonization of spent wood pulping liquor. *ACS Sustainable Chemistry & Engineering*, 6:3385–3391, 3 2018. ISSN 21680485. doi: 10.1021/ACSSUSCHEMENG.7B03582.

[20] John S. McDonald-Wharry, Merilyn Manley-Harris, and Kim L. Pickering. Reviewing, combining, and updating the models for the nanostructure of non-graphitizing carbons produced from oxygen-containing precursors. *Energy and Fuels*, 30:7811–7826, 10 2016. ISSN 15205029. doi: 10.1021/acs.energyfuels.6b00917.

[21] Ying Shao, Chamseddine Guizani, Philippe Grosseau, Didier Chaussy, and Davide Beneventi. Biocarbons from microfibrillated cellulose/lignosulfonate precursors: A study of electrical conductivity develop-

ment during slow pyrolysis. *Carbon*, 129:357–366, 4 2018. ISSN 00086223. doi: 10.1016/j.carbon.2017.12.037.

[22] Singaravelu Vivekanandhan, Manjusri Misra, and Amar Kumar Mohanty. Microscopic, structural, and electrical characterization of the carbonaceous materials synthesized from various lignin feedstocks. *Journal of Applied Polymer Science*, 132:41786, 4 2015. ISSN 1097-4628. doi: 10.1002/APP.41786.

[23] J. Rodríguez-Mirasol, T. Cordero, and J. J. Rodríguez. High-temperature carbons from kraft lignin. *Carbon*, 34:43–52, 1 1996. ISSN 00086223. doi: 10.1016/0008-6223(95)00133-6.

[24] Gang Xiao, Mingjiang Ni, Rui Xiao, Xiang Gao, and Kefa Cen. Catalytic carbonization of lignin for production of electrically conductive charcoal. *Journal of Biobased Materials and Bioenergy*, 6:69–74, 2012. doi: 10.1166/jbmb.2012.1190.

[25] Wei Wang, Romain Lemaire, Ammar Bensakhria, and Denis Luart. Review on the catalytic effects of alkali and alkaline earth metals (AAEMs) including sodium, potassium, calcium and magnesium on the pyrolysis of lignocellulosic biomass and on the co-pyrolysis of coal with biomass. *Journal of Analytical and Applied Pyrolysis*, 163:105479, May 2022. ISSN 0165-2370. doi: 10.1016/j.jaap.2022.105479.

741 [26] Sara Svensson. *Minimizing the sulphur content in Kraft lignin*. PhD thesis,
742 STFI-Packforsk, 2008.

743 [27] Sandip Kumar Singh, Subhrashis Banerjee, Kumar Vanka, and
744 Paresh Laxmikant Dhepe. Understanding interactions between lignin
745 and ionic liquids with experimental and theoretical studies during catalytic
746 depolymerisation. *Catalysis Today*, 309:98–108, 7 2018. ISSN 0920-5861.
747 doi: 10.1016/J.CATTOD.2017.09.050.

748 [28] Ayillath K. Deepa and Paresh L. Dhepe. Lignin depolymerization into aro-
749 matic monomers over solid acid catalysts. *ACS Catalysis*, 5:365–379, 1
750 2015. ISSN 21555435. doi: 10.1021/CS501371Q.

751 [29] Sandip K. Singh, Anthony W. Savoy, Zhaoyang Yuan, Hao Luo, Shannon S.
752 Stahl, Eric L. Hegg, and David B. Hodge. Integrated Two-Stage Alkaline-
753 Oxidative Pretreatment of Hybrid Poplar. Part 1: Impact of Alkaline Pre-
754 Extraction Conditions on Process Performance and Lignin Properties. *Indus-*
755 *trial and Engineering Chemistry Research*, 58(35):15989–15999, sep 2019.
756 ISSN 15205045. doi: 10.1021/acs.iecr.9b01124.

757 [30] Yo Rhin Rhim, Dajie Zhang, D. Howard Fairbrother, Kevin A. Wepasnick,
758 Kenneth J. Livi, Robert J. Bodnar, and Dennis C. Nagle. Changes in elec-
759 trical and microstructural properties of microcrystalline cellulose as func-
760 tion of carbonization temperature. *Carbon*, 48:1012–1024, 4 2010. ISSN
761 00086223. doi: 10.1016/j.carbon.2009.11.020.

[31] A. Ferrari and J. Robertson. Interpretation of raman spectra of disordered and amorphous carbon. *Physical Review B - Condensed Matter and Materials Physics*, 61:14095–14107, 2000. ISSN 1550235X. doi: 10.1103/PhysRevB.61.14095.

[32] Devin McGlamery, Alexander A. Baker, Yi-Sheng Liu, Martín A. Mosquera, and Nicholas P. Stadie. Phonon dispersion relation of bulk boron-doped graphitic carbon. *The Journal of Physical Chemistry C*, 124(42):23027–23037, 2020. doi: 10.1021/acs.jpcc.0c06918.

[33] Seth Kane, Stephan Warnat, and Cecily Ryan. Improvements in methods for measuring the volume conductivity of electrically conductive carbon powders. *Advanced Powder Technology*, 32:702–709, 3 2021. ISSN 0921-8831. doi: 10.1016/J.APT.2021.01.016.

[34] Abdul Awal and Mohini Sain. Spectroscopic studies and evaluation of thermorheological properties of softwood and hardwood lignin. *Journal of Applied Polymer Science*, 122:956–963, 10 2011. ISSN 1097-4628. doi: 10.1002/APP.34211.

[35] E. Jakab, F. Till, T. Székely, and O. Faix. Thermogravimetry/mass spectrometry of various lignosulfonates as well as of a kraft and acetosolv lignin. *Holzforschung*, 45:355–360, 1 1991. ISSN 1437434X. doi: 10.1515/HFSG.1991.45.5.355.

[36] Rhea J. Sammons, David P. Harper, Nicole Labbe, Joseph J. Bozell, Thomas

Elder, and Timothy G. Rials. Characterization of organosolv lignins using thermal and ft-ir spectroscopic analysis. *BioResources*, 8:2752–2767, 2013. URL https://bioresources.cnr.ncsu.edu/resources/characterization-of-organosolv-lignins-using-thermal-and-ft-ir-spectroscopic-analysis/.

[37] National Institute of Standards and Technology. Sodium sulfate, 2021. URL https://webbook.nist.gov/chemistry/.

[38] Santosh M. Bobade, P. Gopalan, and A. R. Kulkarni. Phase transition in na2so4: All five polymorphic transformations in dsc. *Ionics*, 15:353–355, 6 2009. ISSN 09477047. doi: 10.1007/S11581-008-0272-6.

[39] Binod Shrestha, Yann Le Brech, Thierry Ghislain, Sébastien Leclerc, Vincent Carré, Frédéric Aubriet, Sandrine Hoppe, Philippe Marchal, Steve Pontvianne, Nicolas Brosse, and Anthony Dufour. A multitechnique characterization of lignin softening and pyrolysis. *ACS Sustainable Chemistry and Engineering*, 5:6940–6949, 8 2017. ISSN 21680485. doi: 10.1021/ACSSUSCHEMENG.7B01130.

[40] M.M. Nassar and G.D.M. MacKay. Mechanism of thermal decomposition of lignin. *Wood and Fiber Science*, 3, 1984.

[41] Ramesh K Sharma, Jan B Wooten, Vicki L Baliga, Xuehao Lin, W Geoffrey Chan, and Mohammad R Hajaligol. Characterization of chars from py-

rolysis of lignin. *Fuel*, 83(11):1469–1482, August 2004. ISSN 0016-2361. doi: 10.1016/j.fuel.2003.11.015.

[42] Yee Wen Chua, Hongwei Wu, and Yun Yu. Interactions between Low- and High-Molecular-Weight Portions of Lignin during Fast Pyrolysis at Low Temperatures. *Energy & Fuels*, 33(11):11173–11180, November 2019. doi: 10.1021/acs.energyfuels.9b02813.

[43] Chenting Zhang, Yuewen Shao, Lijun Zhang, Shu Zhang, Roel J.M. Westerhof, Qing Liu, Peng Jia, Qingyin Li, Yi Wang, and Xun Hu. Impacts of temperature on evolution of char structure during pyrolysis of lignin. *Science of the Total Environment*, 699:134381, 1 2020. ISSN 18791026. doi: 10.1016/j.scitotenv.2019.134381.

[44] TW Samadhi, LE Jones, and AG Clare. Sox emissions from glass manufacturing: Decomposition of sodium sulfate as influenced by carbon. *Glass Science And Technology-Glastechnische Berichte*, 73(C2):361–369, 2000. ISSN 0946-7475.

[45] Hiromi Aso, Koichi Matsuoka, Atul Sharma, and Akira Tomita. Evaluation of size of graphene sheet in anthracite by a temperature-programmed oxidation method. *Energy and Fuels*, 18:1309–1314, 9 2004. ISSN 08870624. doi: 10.1021/EF030176X.

[46] A. Celzard, J. F. Marêché, F. Payot, and G. Furdin. Electrical conductiv-

ity of carbonaceous powders. *Carbon*, 40(15):2801–2815, jan 2002. ISSN 00086223. doi: 10.1016/S0008-6223(02)00196-3.

[47] SpectraBase. Sodium sulfate anhydrous. URL `https://spectrabase.com/compound/9qW84EFMyGK#4WE3SO8ipx8`.

[48] John McDonald-Wharry. 2013–2014 survey of chars using raman spectroscopy. *C 2021, Vol. 7, Page 63*, 7:63, 8 2021. ISSN 2311-5629. doi: 10.3390/C7030063.

[49] E. R. Buiel, A. E. George, and J. R. Dahn. Model of micropore closure in hard carbon prepared from sucrose. *Carbon*, 37(9):1399–1407, January 1999. doi: 10.1016/S0008-6223(98)00335-2.

[50] J. R. Dahn, W. Xing, and Y. Gao. The "falling cards model" for the structure of microporous carbons. *Carbon*, 35(6):825–830, January 1997. ISSN 0008-6223. doi: 10.1016/S0008-6223(97)00037-7.

[51] Rui Yu, Junxiang Xiang, Kaifa Du, Bowen Deng, Di Chen, Huayi Yin, Ze Liu, and Dihua Wang. Electrochemical Growth of High-Strength Carbon Nanocoils in Molten Carbonates. *Nano Letters*, 22(1):97–104, January 2022. doi: 10.1021/acs.nanolett.1c03284.

[52] Maiyong Zhu, Yu Yang, and Yunping Ma. Salt-assisted synthesis of advanced carbon-based materials for energy-related applications. *Green Chemistry*, 25(24):10263–10303, 2023. doi: 10.1039/D3GC03080F.

[53] Jong Chan Hyun, Hyeong Min Jin, Jin Hwan Kwak, Son Ha, Dong Hyuk Kang, Hyun Soo Kim, Sion Kim, Minhyuck Park, Chan Yeol Kim, Juhee Yoon, Ji Sung Park, Ji-Young Kim, Hee-Dae Lim, Se Youn Cho, Hyoung-Joon Jin, and Young Soo Yun. Design guidelines for a high-performance hard carbon anode in sodium ion batteries. *Energy & Environmental Science*, 17(8):2856–2863, April 2024. doi: 10.1039/D4EE00315B.